

Automated detection of corrosion in used nuclear fuel dry storage canisters using residual neural networks

Theodore Papamarkou^a, Hayley Guy^b, Bryce Kroenke^c, Jordan Miller^d, Preston Robinette^e, Daniel Schultz^f, Jacob Hinkle^a, Laura Pullum^g, Catherine Schuman^g, Jeremy Renshaw^h, Stylianos Chatzidakisⁱ

^a*Computational Sciences and Engineering Division, Oak Ridge National Laboratory, Oak Ridge, Tennessee, USA*

^b*Department of Mathematics, North Carolina State University, Raleigh, North Carolina, USA*

^c*Department of Computer Science, University of California, Davis, California, USA*

^d*Center for Cognitive Ubiquitous Computing, Arizona State University, Tempe, Arizona, USA*

^e*Presbyterian College, Clinton, South Carolina, USA*

^f*Innovative Computing Laboratory, University of Tennessee, Knoxville, Tennessee, USA*

^g*Computer Science and Mathematics Division, Oak Ridge National Laboratory, Oak Ridge, Tennessee, USA*

^h*Electric Power Research Institute, Palo Alto, California, USA*

ⁱ*Reactor and Nuclear Systems Division, Oak Ridge National Laboratory, Oak Ridge, Tennessee, USA*

Abstract

Nondestructive evaluation methods play an important role in ensuring component integrity and safety in many industries. Operator fatigue can play a critical role in the reliability of such methods. This is important for inspecting high value assets or assets with a high consequence of failure, such as aerospace and nuclear components. Recent advances in convolutional neural networks can support and automate these inspection efforts. This paper proposes using residual neural networks (ResNets) for real-time detection of corrosion, including iron oxide discoloration, pitting and stress corrosion cracking, in dry storage stainless steel canisters housing used nuclear fuel. The proposed approach crops nuclear canister images into smaller tiles, trains a ResNet on these tiles, and classifies images as corroded or intact using the per-image count of tiles predicted as corroded by the ResNet. The results demonstrate that such a deep learning approach allows to detect the locus of corrosion via smaller tiles, and at the same time to infer with high accuracy whether an image comes from a corroded canister. Thereby, the proposed approach holds promise to automate and speed up nuclear fuel canister inspections, to minimize inspection costs, and to partially replace human-conducted onsite inspections, thus reducing radiation doses to personnel.

Keywords: convolutional neural networks, corrosion, deep learning, dry storage canisters, feature detection, residual neural networks.

1. Introduction

Dry storage systems housing used nuclear fuel from commercial nuclear power reactors (Figure 1) will be used for longer periods than initially anticipated and there is a concern that some of these systems may become vulnerable to physical degradation, e.g., pitting and chloride-induced stress corrosion cracking (SCC). The potential for SCC at the heat af-

fected zones of welded stainless-steel interim storage canisters has been identified by several agencies [1, 2, 3, 4, 5, 6, 7, 8]. Although this concern has motivated the development of delivery systems and inspection of these canisters on a regular basis [9, 10, 11, 12, 13, 14, 15, 16, 17, 18, 19, 20, 21, 22, 23, 24, 25], the large number of stored canisters that need to be visually inspected (currently approximately 3,200

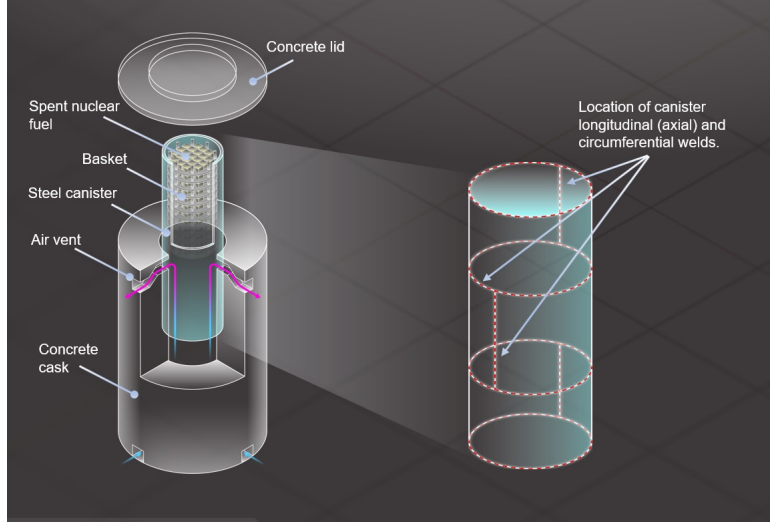


Figure 1: Illustration of a vertical used nuclear fuel dry storage system. This figure is for illustration purposes and does not attempt to depict a specific design. There is a large variation in design characteristics, which is not possible to capture in a figure, e.g., dry storage systems that use a steel overpack for shielding instead of a concrete one or stainless steel canisters made by welding two cylindrical sections instead of three.

canisters have been installed in the U.S. and projections show that eventually over 10,000 canisters will be required by 2050 [26]), high radiation levels, limited access (through small size vents) and space constraints (overpack-canister gap less than 5-10 centimeters) make in-situ visual inspections challenging. This necessitates the development of remotely operated systems for real-time detection of flaws including type, location, size, and density, to support future remediation activities, reduce operator errors, and optimize repair quality. As a result, an integrated deep learning framework that would allow scanning a larger area and with high detection capabilities would be a big step forward to reduce dose-rate to operators, minimize inspection costs, and ensure long-term safety of used nuclear fuel canisters.

Existing methods for detecting structural defects in images include Frangi filters and Hessian affine region detectors [27], total variation denoising [28, 29], combinations of image processing techniques for feature extraction [30, 31] with machine learning algorithms for classification [32, 33], and more lately deep convolutional neural networks (CNNs) [34, 35]. So

far, no deep learning approaches have been used to address inspection of used nuclear fuel canisters. Radiation levels typically create noise, flacking, snowing and other artifacts in cameras. Such artifacts pose a challenge for conventional feature detection techniques, e.g., shallow neural networks, that rely on clean surfaces, isolated defects, and radiation-free viewing with optimal lighting conditions. So, the process of inspecting used nuclear fuel canisters is not automated algorithmically and it induces a challenging image classification problem. Deep learning is a plausible approach for automating such a challenging classification problem. In fact, [35] have applied CNNs for detecting concrete cracks in radiation-free civil infrastructures. Along the lines of [35], this paper crops images to smaller tiles to train the underlying CNN.

The proposed approach is differentiated from [35] in three ways. Firstly, ResNets are used for detecting corrosion instead of deploying a custom CNN architecture. Training three different ResNets (ResNets-18, ResNet-34 and ResNet-50) demonstrates that the proposed approach tackles the corrosion detec-

tion problem without being sensitive to the choice of ResNet architecture. Secondly, the present paper introduces a classification rule for identifying images as corroded or intact using ResNets trained on tiles cropped out of these images. This way, the locations of potential corrosion are linked to tiles predicted as corroded, while at the same time the problem of classifying the original images is solved with high prediction accuracy without being sensitive to tile-specific prediction errors. Finally, the proposed approach is focused on the specific application of detecting corrosion in real data imagery similar to used nuclear fuel canisters.

CNNs have been applied for detecting cracks in videos of nuclear power plants [36]. The proposed approach differs from [36] in four aspects. Firstly, data have been collected from nuclear fuel canisters, and not from nuclear power plants. Secondly, the EPRI data consist of images (spatial information), and not of videos (spatiotemporal information). Thirdly, the classification problem in this paper is to decide whether each image contains any sign of corrosion, whereas the classification problem in [36] is to decide whether tubelets extracted from multiple video frames contain corrosion cracks. Fourthly, this paper employs ResNets for tile classification in conjunction with a custom image classification rule, whereas [36] employs a custom CNN architecture for crack patch detection per frame along with a three-step data fusion algorithm for generating bounding boxes around detected crack tubelets.

2. Materials and methods

2.1. Data

The research presented in this paper is based on data provided by the Electric Power Research Institute (EPRI). The data consist of 166 images taken from flaw mockup specimens produced by EPRI. These images, which capture stainless-steel canister surfaces, were taken with a 16-megapixel camera from a variety of locations, angles, and lighting conditions to induce high variability in the dataset. Each image has a $4,928 \times 3,264$ -pixel resolution. Figure 2 shows an example corroded image. Interest is in detecting

corrosion in the images. The images contain stress corrosion cracks with and without iron oxide discoloration. Interest is in detecting pitting or stress corrosion cracks independent of iron oxide discoloration in the images.

Use of deep learning for detecting nuclear canister corrosion requires training sets of sample size larger than the 166 available images. For this reason, the 166 images were cropped into smaller tiled images of 256×256 -pixel resolution using a custom-made algorithm for this task, producing a total of 37,719 tiled images (referred to as tiles thereafter). Each tile was labeled either as corroded or as intact, depending on whether it contains any signs of corrosion (including iron oxide discoloration, pitting, and stress corrosion cracks with or without iron oxide discoloration) or not. Thus, the ground truth for image annotation takes into account only corrosion identifiable via the naked human eye. The generated dataset of tiles includes a broad range of image variations (see Figure 3), which are necessary for CNN training.

The 256×256 -pixel resolution for tiles was chosen empirically. Such a small resolution facilitates the training process of CNNs with tiled images coming from original images of varied resolution, therefore making the approach camera-independent and more generally applicable. On the other hand, tiles of smaller resolution may lead CNNs to mistake elongated features, such as scratches, for cracks. In addition, smaller tiles render their labeling less obvious to the human eye.

4,957 out of the 37,719 tiles were manually labeled as corroded, while the remaining 32,762 were labeled as intact. After manually labeling each tile either as corroded or as intact, the dataset of tiles was split randomly into a training, validation, and test set, containing 22,215, 7,538, and 7,966 tiles, respectively, thus attaining a 60% – 20% – 20% split. In order to keep the training, validation, and test sets independent, tiles from a particular image were included in only one set. Table 1a shows the number of corroded and intact original images while Table 1b shows the number of corroded and intact tiles in each of the three sets. An original image is corroded if it contains at least one tile manually labeled as corroded, otherwise it is intact. It is noted that the



Figure 2: Example image with visible corrosion, stress corrosion cracks, and artifacts (scratches, shadows, etc.). Note: this is a laboratory corroded stainless steel sample and not an image from an actual used fuel canister; to the best of our knowledge no canisters have been detected with defects).

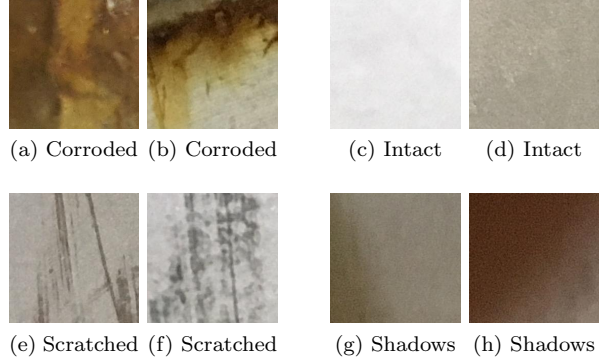


Figure 3: Examples of 256×256 -pixel resolution tiles used for training, which demonstrate the large variability in the dataset. Tiles with with corrosion, including iron oxide discoloration, pitting or stress corrosion cracks (with or without iron oxide discoloration) (3a-3b) are labeled as corroded, while tiles without defects (3c-3d) or with scratches (3e-3f) or shadows (3g-3h) are labeled as intact.

	Corroded	Intact	Total
Training	50	49	99
Validation	17	17	34
Test	17	16	33
Total	84	82	166

(a) Dataset of original images

	Corroded	Intact	Total
Training	2,898	19,317	22,215
Validation	1,235	6,303	7,538
Test	824	7,142	7,966
Total	4,957	32,762	37,719

(b) Dataset of tiles

Table 1: Total number of images and number of corroded and intact images per set in the original dataset of images (1a), from which the tiles were extracted, and in the generated dataset of tiles (1b). Rows represent datasets and columns represent classes.

60% – 20% – 20% split between training, validation, and test set is preserved at the level of original images too (99, 34 and 33 original images in the respective sets).

2.2. Brief overview of CNNs

The first computational model for neural networks were conceived in the 1940s [37]. Hebian networks were simulated by [38] and perceptrons were created by [39] in the 1950s. The neocognitron, the origin of the CNN architecture, was introduced by [40] in the 1980s. The neocognitron introduced two basic layer types in CNNs, namely convolutional layers and

downsampling layers. LeNet, a CNN developed by [41, 42] in the 1990s to recognize hand-written zip code numbers, led to the emergence of CNNs and laid the foundations of modern computer vision.

A feed-forward CNN consists of multiple layers of units, starting with an input layer, followed by combinations of convolution, pooling, activation and fully connected layers, and ending with an output layer (see Figure 4). Convolution layers perform convolution operations to extract high level features from the input image. Convolution operations preserve the spatial relationship between pixels by learning image features using small squares of input data. Each

convolution layer is typically followed by a unit-wise activation function, such as the rectified linear unit (ReLU). Pooling layers reduce the dimensionality of each extracted feature, but they retain the most important information. In a fully connected layer, each neuron is connected to every neuron in the previous layer. Fully connected layers learn non-linear combinations of the features identified by the convolutional layers. A common final layer in CNNs is the softmax layer, which assigns probabilities to each class label. For a more detailed introduction to CNNs, see for example [43].

CNNs are prominent tools for image classification for several reasons. In particular, CNNs

- are universal function approximators [44],
- attain high predictive accuracy in comparison to other machine learning algorithms,
- automate feature extraction from input data while preserving the spatial relationship between pixels,
- reduce the number of parameters via the convolution operator relatively to fully connected artificial neural networks, and
- allow transfer of knowledge across different domains.

The capacity of CNNs to transfer knowledge across different domains is known as transfer learning [45]. In practice, transfer learning entails the following steps; a CNN is trained on a dataset related to some problem, the knowledge acquired (such as the CNN weights and biases) is stored, and the stored knowledge for this pre-trained CNN is used for fine tuning the CNN on a dataset related to a different, yet usually relevant, problem. In transfer learning, some components (such as weights or biases) of a CNN are typically fixed (frozen) to values obtained by pre-training on some dataset, while new layers or components attached to the pre-trained CNN are trained on a new dataset.

2.3. Proposed algorithm

In this paper, ResNets are used, which are a specific type of CNN architecture [46]. The last (output) layer of ResNets is a fully connected layer of 1,000 units. Since this paper deals with the binary classification problem of whether each image is corroded

or intact, the last fully connected ResNet layer of 1,000 units is replaced by a fully connected layer of 2 units. The ResNet backbone preceding the replaced last layer is not frozen. This means that the weights and biases of the ResNet backbone are not fixed to some pre-trained values, therefore transfer learning is not employed. Instead, the modified CNN architecture, arising from the altered last ResNet layer, is trained by randomly initializing the weights and biases of all layers.

At a greater level of detail, the last fully connected layer of 1,000 units is replaced by a layer that concatenates adaptive average pooling and adaptive max pooling, a flattening layer and a fully connected layer of 2 units. The implementation is based on the `fastai` library. More details can be found in the documentation of the `cnn_learner` method of `fastai` and in the accompanying code of this paper (see Section 2.4).

Each of the 7,719 tile images in the generated dataset is passed to the ResNet input layer as a $256 \times 256 \times 3$ tensor, whose three dimensions correspond to tile height, width and RGB channel (red, green and blue), respectively. The prediction made at the ResNet output layer indicates whether the input tile is considered to be corroded or intact. Raw images are cropped into tiles, which are in turn manually labeled and split into training, validation and test set. After training the ResNet on the training set, predictions are made for tiles coming from the test set. The heatmap of Figure 5 visualizes the tile predictions made by the ResNet, with red-colored and green-colored tiles predicted as corroded and intact, respectively.

The posed research question is to classify images as corroded or intact, whereas a ResNet provides predictions for fragments of the image. To solve the original problem, a rule for image classification can be defined by utilizing tile predictions. One classification rule is to predict the original image as corroded if it contains at least one tile predicted as corroded. However, such a classification rule is prone to produce false alarms due to being sensitive to tile prediction errors. Misclassifying a single tile as corroded is sufficient to produce a false alarm for the original image.

To make corrosion detection for an image less sus-

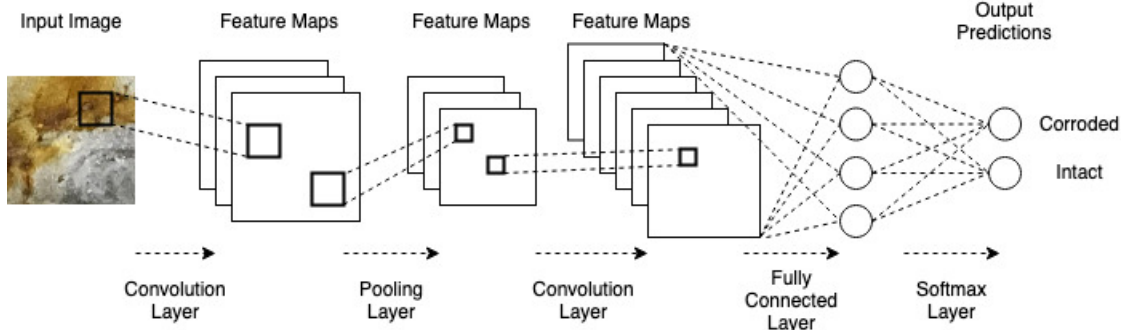


Figure 4: Visual representation of a typical feed-forward CNN architecture.

ceptible to its constituent misclassified tiles, the classification of the image can be defined by considering the absolute frequency of misclassified tiles. Let n_i be the number of tiles in the i -th image and $\hat{y}_t^{(i)}$ the prediction made by the ResNet for tile t in image i . The prediction $\hat{y}^{(i)}$ for image i is set to

$$\hat{y}^{(i)} = \begin{cases} 1, & \text{if } \sum_{t=1}^{n_i} \hat{y}_t^{(i)} > c, \\ 0, & \text{otherwise.} \end{cases} \quad (1)$$

assuming that 1 and 0 correspond to presence and absence of corrosion, and c is a hyper-parameter.

The hyperparameter c sets a threshold on the count of tiles predicted as corroded, above which the image consisting of these corroded tiles is predicted to be corroded itself. This classification rule has been instigated by training ResNets on tiles. It has been observed empirically that images with pitting or stress corrosion cracks tend to contain higher number of corroded tiles than intact images with fewer (or no) tiles misclassified as corroded.

A value for the hyper-parameter c can be chosen by optimizing a performance metric, such as prediction accuracy per image, on the validation set. More specifically, if $M(\{\hat{y}^{(i)}(c) : i\})$ is a performance metric, viewed as a function of image predictions $\{\hat{y}^{(i)}(c) : i\}$ dependent on c and made over the validation set, then c can be estimated by $\hat{c} = \sup_c M(\{\hat{y}^{(i)}(c) : i\})$.

To summarize, the proposed algorithm for detecting whether an image contains corrosion comprises

the following steps:

1. Run a ResNet on the validation set of tiles to tune hyperparameters relevant to training, such as the learning rate for stochastic gradient descent.
2. Train the ResNet on the training set of tiles.
3. Tune the value of hyperparameter c using the validation set of tiles. To do so, predict the labels of tiles in the validation set via the trained ResNet, use these tile predictions to compute the whole image predictions via equation (1) for various values of c , and select the value of c that maximizes a performance metric, such as the prediction accuracy or F1 score.
4. Predict the labels of images in the test set. To do so, predict the labels of tiles in the test set via the trained ResNet, and use these tile predictions to compute the whole image predictions via equation (1) for the value of c obtained at step 3.

As it can be seen from the described algorithm, a new image is cropped into tiles, its tiles are predicted as corroded or intact via the trained ResNet, and equation (1) is used for predicting whether the image is corroded or intact.

2.4. Tuning, training and implementation

This section provides details of hyperparameter tuning, of the configuration of the training process and of the implementation. To start with, data augmentation was performed on the training and validation sets by carrying out random rotations, flips,

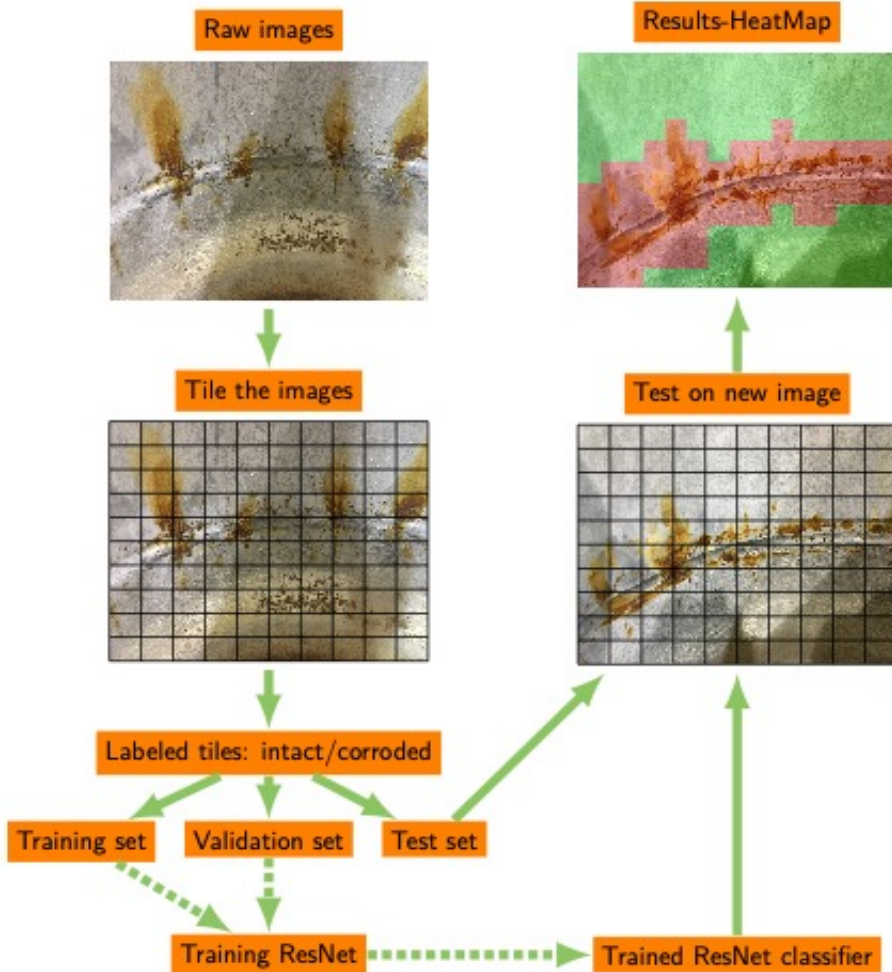


Figure 5: Flowchart for classifying tiles using a ResNet. Solid lines represent training steps and dashed lines refer to test steps. Tiles from the test set, stitched back together to display the image of origin, are colored as red or green depending on whether they have been predicted as corroded or as intact by the ResNet.

color shifting, zooming and symmetric warping of the tiled images.

An 18-layer, a 34-layer, and a 50-layer ResNet were employed in order to validate the discriminative power of the proposed approach to corrosion detection regardless of the deployed ResNet architecture (see [46] for the definitions of ResNet-18, ResNet-34 and ResNet-50). The last fully connected layer of 1,000 units in each of these three ResNets was re-

placed by a fully connected layer of 2 units. From this point onwards, every reference to ResNet-18, ResNet-34 and ResNet-50 alludes to the respective ResNets with modified last layers.

A mock training session with the learning rate finder of [47] was run on the validation set for each ResNet. The learning rate was tuned across all layers, since the ResNet backbone was not kept frozen. Figure 6a displays an example of a loss curve plotted

against the range of learning rates used in a mock run of the learning rate finder on ResNet-34. According to Figure 6a, the loss curve has a downward slope in the interval $[10^{-6}, 10^{-1}]$. Following common practice, a value approximately in the middle of the sharpest downward slope, such as $5 \cdot 10^{-4}$, is chosen as the learning rate upper bound.

After tuning the learning rate, discriminative layer training using the one-cycle policy of [48] was performed. Discriminative layer training refers to the process of training with different learning rates across layers. On the basis of Figure 6a, the learning rate range for discriminative layer training was set to the interval $[10^{-6}, 5 \cdot 10^{-4}]$. This way, the learning rates for the first and last layer of each ResNet were set to 10^{-6} and to $5 \cdot 10^{-4}$ during training, respectively, with the intermediate layers having learning rates logarithmically distributed between 10^{-6} and $5 \cdot 10^{-4}$.

Each ResNet was trained by running the one-cycle policy [48] for 50 epochs. Training was run for batch sizes of 32, 64, 128 and 256 for each of the three ResNets. The training and validation loss curves were similar across different batch sizes and different ResNets. For example, Figures 6c and 6d show a similar pattern of training and validation loss curves for ResNet-34, and for respective batch sizes of 32 and 128.

The threshold c of equation (1) for image classification was selected by maximizing the F1 score of image predictions on the validation set (see Section 3 for more details about the F1 score). Figure 6b provides an example of an F1 score curve, showing F1 values for a range of c values. It is noted that threshold c is selected to maximize accuracy and does not translate to a corrosion threshold. Whether an image is corroded or not is determined by acceptance criteria mandated by acceptable industry standards. However, different acceptance criteria will result in training sets with different corroded/intact partitions and subsequently in different values of threshold c .

A Python package, called `nccd`, accompanies this paper. It is publicly available at

<https://github.com/papamarkou/nccd>

and it comes with an example of running the proposed algorithm. ResNet training and tile predictions

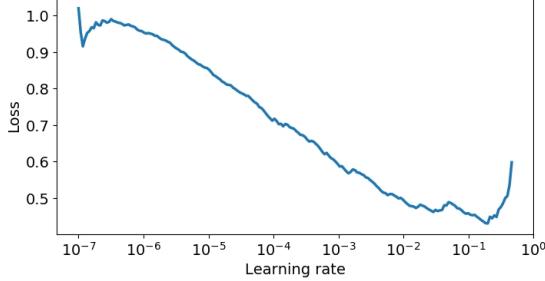
in `nccd` make use of the `fastai` library. The `nccd` package implements the classification rule of equation (1) for making image predictions based on tile predictions. More generally, `nccd` automates the process of running the proposed algorithm. The EPRI data used in the analysis are proprietary, therefore they are not available in the public domain.

Simulations were run on an NVIDIA Tesla V100 GPU of a DGX-1 server at the CADES Cloud at Oak Ridge National Laboratory (ORNL). The training runtime for 50 epochs using the one-cycle policy varied from 40 minutes for ResNet-18 to 115 minutes for ResNet-50.

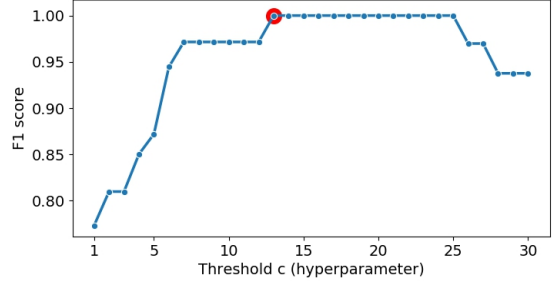
3. Results

This section provides performance metrics on the basis of tiled image predictions made by the three ResNets and on the basis of whole image predictions made via equation (1). All predictions were made on the test set. Tables 2a and 2b show numerical performance metrics, namely true negatives (TN; intact correctly predicted as intact), false positives (FP; intact wrongly predicted as corroded), false negatives (FN; corroded wrongly predicted as intact), true positives (TP; corroded correctly predicted as corroded), true positive rates (TPR), false positive rates (FPR), positive predictive values (PPV), prediction accuracies (ACC) and F1 scores. The definition of these metrics are available in the Appendix. Moreover, Figure 7 displays visual performance metrics, namely receiver operating characteristic (ROC) curves, which are plots of TPR against FPR.

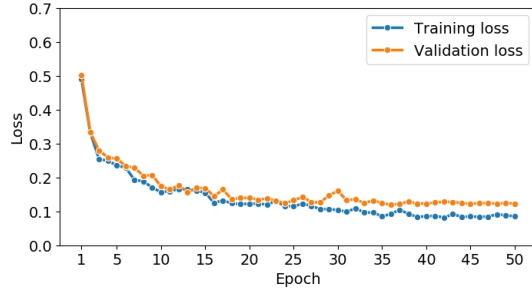
Tiled image predictions (on the test set) are similar across different batch sizes. For example, the ROC curves for ResNet-34 based on four batch sizes (32, 64, 128 and 256) are nearly identical (Figure 7a). As another example, the ROC curves across the three ResNets for batch size equal to 128 are nearly identical (Figure 7b). It is reminded that the training and validation loss curves (based on the training and validation set) are also similar across different batch sizes (see Figures 6c and 6d). In summary, neither the choice of ResNet nor the choice of batch size seem to have a drastic effect on tiled image predictive capacity. On the other hand, a batch size of 128 yields



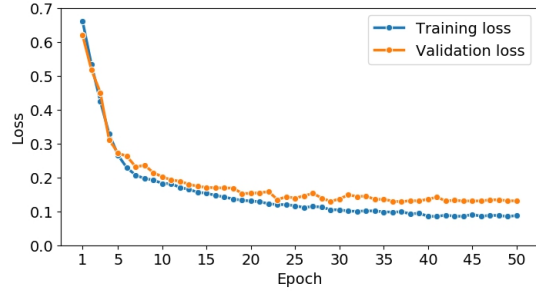
(a) Loss vs learning rate; ResNet-34, batch size 128



(b) F1 score vs c ; ResNet-34, batch size 128

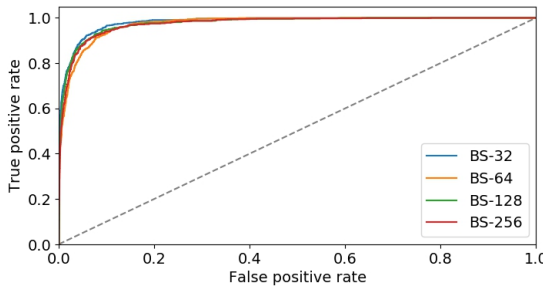


(c) Loss vs epoch; ResNet-34, batch size 32

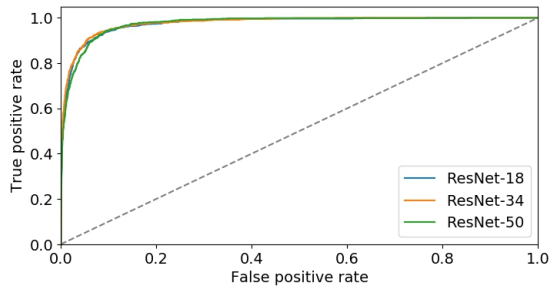


(d) Loss vs epoch; ResNet-34, batch size 128

Figure 6: Diagnostic plots related to ResNet tuning and training. (6a): plot of loss versus learning rate from a mock training session with the learning rate finder of [47]. The training session was run using ResNet-34 and a batch size of 128. The loss has the sharpest downward slope in the vicinity of $5 \cdot 10^{-4}$, so the learning rate interval $[10^{-6}, 5 \cdot 10^{-4}]$ is a plausible choice for discriminative layer training. (6b): plot of F1 score versus hyperparameter c . Tiled image predictions were made on the validation set via ResNet-34 using a batch size of 128. The tiled image predictions were then used for making whole image predictions via equation (1) for $c = 1, 2, \dots, 30$. The F1 score was computed for the image predictions arising from each value of c . $\hat{c} = 13$ is chosen as the threshold value maximizing the F1 score (see red-colored point). (6c) and (6d): plots of training and validation loss versus epoch obtained by training ResNet-34 with the one-cycle policy of [48] for batch sizes of 32 and of 128, respectively. The two batch sizes yield similar training and validation loss curves.



(a) ROC curves; ResNet-34, four batch sizes



(b) ROC curves; batch size of 128, three ResNets

Figure 7: ROC curves are nearly identical for different ResNets and for different batch sizes. All ROC curves were generated using the test set.

	ResNet-18	ResNet-34	ResNet-50
TN	7004	6936	6938
FP	138	206	204
FN	205	143	190
TP	619	681	634
TPR	0.7512	0.8265	0.7694
FPR	0.0193	0.0288	0.0286
PPV	0.8177	0.7678	0.7566
ACC	0.9569	0.9562	0.9505
F1	0.7830	0.7960	0.7629

(a) Performance metrics for tiled images

	ResNet-18	ResNet-34	ResNet-50
TN	16	15	14
FP	0	1	2
FN	1	1	0
TP	16	16	17
TPR	0.9412	0.9412	1
FPR	0.0000	0.0625	0.1250
PPV	1.0000	0.9412	0.8950
ACC	0.9697	0.9394	0.9394
F1	0.9697	0.9412	0.9444

(b) Performance metrics for whole images

Table 2: Performance metrics for assessing the quality of classification of tiled images (2a) and of whole images (2b) as corroded or intact using three ResNets and a batch size of 128. The first, second and third column in each table correspond to ResNet-18, ResNet-34 and ResNet-50. TN, FP, FN, TP, TPR, FPR, PPV, ACC, and F1 stand for true negative, false positive, false negative, true positive, true positive rate, false positive rate, positive predictive value, prediction accuracy and F1 score, respectively. The performance metrics were evaluated on the basis of tiled and whole image predictions made on the test set.

more accurate whole image predictions (on the EPRI test set) than batch sizes of 32, 64 and 256. For this reason, the metrics of Tables 2a and 2b pertain to predictions based on a batch size of 128.

Both ACC and F1 are plausible candidates for tuning the threshold c in equation (1) for the available data, since the classes of intact and corroded images are balanced with a sample size ratio of $82/84 \approx 1$ (see Table 1a). The F1 score would be preferred over ACC for tuning hyperparameter c in equation (1) in the case of imbalanced classes of intact and of corroded images. As seen in Table 2a, the respective accuracies ACC of tile predictions for ResNet-18, ResNet-34 and ResNet-50 are 95.69%, 95.62% and 95.05%, while the respective F1 scores of tile predictions are 78.30%, 79.60% and 76.29%. The lower F1 scores in comparison to accuracies are related to the class imbalance between corroded and intact tiles. The probabilities of corrosion detection (TPR) correspond to 75.12%, 82.65% and 76.94%, while the probabilities of false alarms (FPR) correspond to 1.93%, 2.88% and 2.86% for ResNet-18, ResNet-34 and ResNet-50. Overall, tiled image predictive performance is similar across the three ResNet architectures according to Table 2a.

Moreover, the image classification rule based on

equation (1) is not sensitive to the choice of ResNet architecture according to Table 2b. More specifically and at whole image-level, ResNet-18, ResNet-34 and ResNet-50 combined with the image classifier of equation (1) yield respective prediction accuracies of 96.97%, 93.94% and 93.94%, F1 scores of 96.97%, 94.12% and 94.44%, probabilities of corrosion detection (TPR) of 94.12%, 94.12% and 100%, and probabilities of false alarm (FPR) of 0%, 6.25% and 12.50%. Thereby, Table 2b provides empirical evidence that the image classifier of equation (1) is not sensitive to tile misclassification errors or to the choice of ResNet architecture for tile classification.

So, this paper provides a first empirical indication that the algorithm of Section 2.3 can be used to automatically detect corrosion in the test images provided by EPRI. At the same time, it is emphasized that the EPRI test set consists of 33 images only (see Table 1a). A larger dataset would help to train, tune and test the proposed approach more extensively in the future. Moreover, datasets collected from alternative sites would help to assess the capacity of the proposed approach to identify corrosion on spent fuel storage canisters with varying characteristics or from varying locations.

A graphical user interface (GUI) was developed us-

ing PyQt to automate the process and analyze images. The GUI provides a colormap that highlights any identified corroded and intact areas within the image and provides additional information to the operator including percentage of image that is corroded. Figure 8 demonstrates GUI usage via an image classified as corroded. It is noted that this image was particularly challenging with a lot of artifacts (shadows, scratches, etc.). However, the proposed deep learning approach captured correctly all the corroded areas (highlighted with yellow color).

4. Discussion and conclusions

This paper proposes an image classification algorithm based on deep learning for detecting corrosion, including discoloration, pitting, and stress corrosion cracks, in stainless steel canisters. Despite the small sample size of 166 EPRI images, the algorithm attains high predictive accuracy on the EPRI test set and therefore encourages further experimentation and investigation towards future deployment as an operator decision support system intended to augment existing human inspector capabilities for detecting corrosion in used nuclear fuel canisters. The proposed algorithm trains a ResNet on a training set of tiles, tunes the value of hyperparameter c using the validation set of tiles, and then uses tile predictions to compute whole image predictions. The proposed image classifier is highly performing on the small EPRI test set of 33 images and not sensitive to tile misclassification errors or to the choice of ResNet architecture for tile classification. Thus, the proposed algorithm holds promise for addressing the research question of automatically detecting corrosion in used fuel nuclear canisters.

Future work includes a more exhaustive testing by acquiring a larger dataset of images from a diverse collection of corroded and intact samples and by allowing for class imbalances at whole image-level. Variations of the classification rule of equation (1) can be considered, for example by introducing sliding window techniques across tiles to take into account spatial information in tile predictions along with tile prediction counts. Another future direction would

be to attempt pixel-wise labelling instead of cropping into 256×256 tiles, followed by a pixel-centric classification rule instead of the tile-centric classification rule of equation (1). Such an approach would require of an upfront investment to annotate images pixel-wise. A preliminary attempt to assess the proposed approach using video input instead of image input has been made, which takes about 15 seconds for ResNet training per input file. To enable real-time usage with video input, future work will use optical flows. Video files are not efficient for solving the corrosion classification problem because consecutive frames contain redundant information as the camera pans. Optical flows eliminate this issue and allow for the entire canister to be visualized by a single image. Thus, the proposed algorithm will be evaluated on images derived from optical flows.

Appendix A. Performance metrics

A tiled image prediction or an original image prediction is characterized as positive if it is corroded (labeled as 1), and as negative if it is intact (labeled as 0). TPR is defined as

$$TPR = TP/(TP + FN),$$

it provides the probability of detection of corroded images, and it is therefore crucial for assessing corrosion detection in nuclear canisters. FPR is defined as

$$FPR = FP/(FP + TN),$$

and gives the probability of false alarm. PPV is defined as

$$PPV = TP/(TP + FP),$$

and is particularly useful in the context of tile predictions, since the classes of intact and of corroded tiles are imbalanced with a sample size ratio of $37,762/4,957 \approx 7/1$ (see Table 1b). The F1 score is defined as

$$F1 = 2 \times PPV \times TPR / (PPV + TPR),$$

and it is the harmonic mean of FPR and PPV. The overall prediction accuracy is given by

$$ACC = (TP + TN) / (TP + TN + FP + FN).$$

A ROC curve is a plot of TPR against FPR.

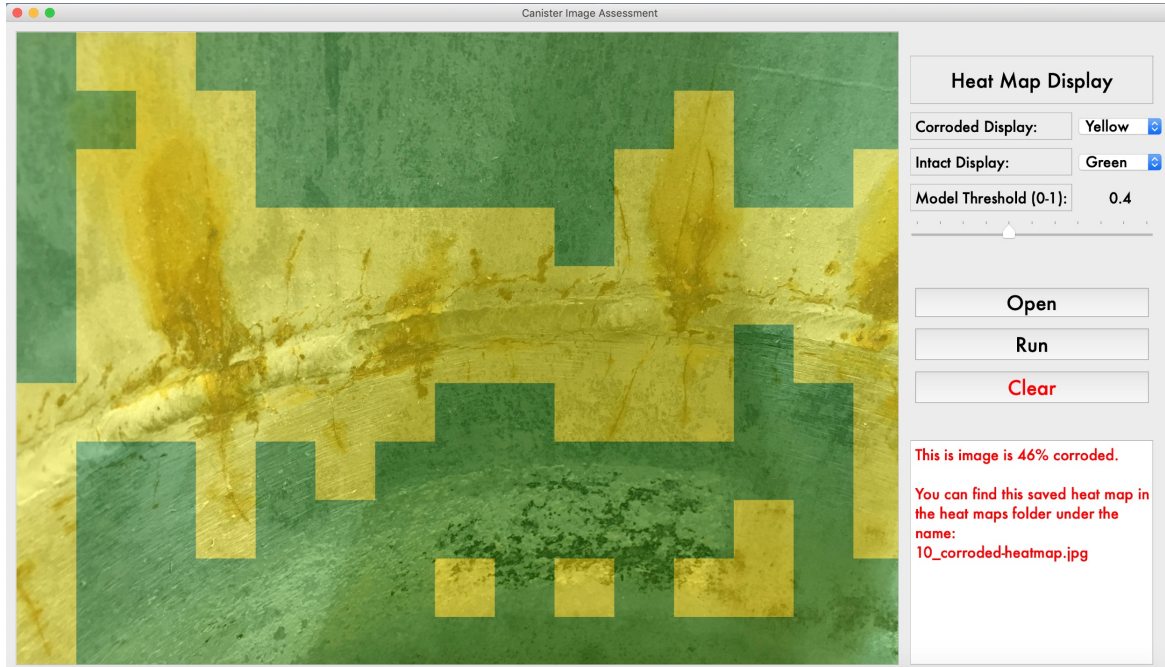


Figure 8: Visualization of an image identified as corroded using the GUI. The corroded areas are highlighted using yellow color and intact areas using green color.

Acknowledgements

This manuscript has been authored by UT Battelle, LLC, under contract DE-AC05-00OR22725 with the US Department of Energy (DOE). The US government retains and the publisher, by accepting the article for publication, acknowledges that the US government retains a nonexclusive, paid-up, irrevocable, worldwide license to publish or reproduce the published form of this manuscript, or allow others to do so, for US government purposes. DOE will provide public access to these results of federally sponsored research in accordance with the DOE Public Access Plan (<http://energy.gov/downloads/doe-public-access-plan>).

This work was funded by the AI Initiative at the Oak Ridge National Laboratory.

This research used resources of the Compute and Data Environment for Science (CADES) at the Oak Ridge National Laboratory, which is supported by the Office of Science of the U.S. Department of Energy under Contract No. DE-AC05-00OR22725.

The authors would like to thank Guannan Zhang for helping with the co-supervision of the nuclear project interns at the artificial intelligence summer institute (AISI) 2019 of ORNL.

References

- [1] J. Kusnick, M. Benson, S. Lyons, Finite element analysis of weld residual stresses in austenitic stainless steel dry cask storage system canisters, Tech. rep. (2013).
- [2] D. B. Rigby, Evaluation of the technical basis for extended dry storage and transportation of used nuclear fuel: executive summary, US Nuclear Waste Technical Review Board, 2010.
- [3] B. Hanson, H. Alsaed, C. Stockman, D. Enos, R. Meyer, K. Sorenson, Gap analysis to support extended storage of used nuclear fuel (rev.0),

Tech. rep., US Department of Energy Used Fuel Disposition Campaign (2012).

[4] O. K. Chopra, D. R. Diercks, R. R. Fabian, Z. H. Han, Y. Y. Liu, Managing aging effects on dry cask storage systems for extended long-term storage and transportation of used fuel (rev. 2), Tech. rep., Argonne National Laboratory, Argonne, IL (2014).

[5] S. Chu, Flaw growth and flaw tolerance assessment for dry cask storage canisters (2014).

[6] J. Gorman, Fuhr K., Broussard J., Literature Review of Environmental Conditions and Chloride-Induced Degradation Relevant to Stainless Steel Canisters in Dry Cask Storage Systems, Tech. rep., Electric Power Research Institute, Palo Alto, CA (2014).

[7] Fuhr K., Broussard J., White G., Aging management guidance to address potential chloride-induced stress corrosion cracking of welded stainless steel canisters, Tech. rep., Electric Power Research Institute, Palo Alto, CA (2017).

[8] J. Broussard, S. Chu, Susceptibility assessment criteria for chloride-induced stress corrosion cracking (CISCC) of welded stainless steel canisters for dry cask storage systems, Tech. rep., Electric Power Research Institute, Palo Alto, CA (2015).

[9] R. M. Meyer, Nondestructive examination guidance for dry storage casks, Tech. Rep. September, Pacific Northwest National Laboratory (2016).

[10] R. M. Meyer, NDE to manage atmospheric SCC in canisters for dry storage of spent fuel, Tech. rep., Pacific Northwest National Laboratory (2013).

[11] J. Renshaw, S. Chu, Dry canister storage system inspection and robotic delivery system development, in: Transactions of the American Nuclear Society, Vol. 115, Palo Alto, CA, 2016, pp. 199–200.

[12] S. Chu, Dry cask storage welded stainless steel canister breach consequence analysis, Tech. rep., Electric Power Research Institute, Palo Alto, CA (2019).

[13] Bryan C., Enos D., Diablo Canyon Stainless Steel Dry Storage Canister Inspection, Tech. rep., Electric Power Research Institute, Palo Alto, CA (2016).

[14] W. Tang, S. Chatzidakis, R. Miller, J. Chen, D. Kyle, J. Scaglione, C. Schrad, Welding process development for spent nuclear fuel canister repair, in: American Society of Mechanical Engineers, Pressure Vessels and Piping Division (Publication) PVP, Vol. 1, 2019. doi: 10.1115/PVP2019-93946.

[15] J. M. Chatzidakis, Stylianatos and Adeniyi, Abiodun Idowu and Severynse, Tom F and Jones, Robert and Jarrell, Joshua and Scaglione, A novel mobile examination and remediation facility for On-site remediation of dry storage systems, in: Proceedings of the Waste Management Conference, Phoenix, AZ, 2018.

[16] J. J. Stylianatos Chatzidakis, Efe Kurt, Justin Coleman, John M Scaglione, System-wide impacts of resolution options for a nonconforming dry storage system, in: Proceedings of Global/TopFuel 2019, Seattle, Washington, 2019, pp. 1040–1047.

[17] S. Chatzidakis, Neutron diffraction illustrates residual stress behavior of welded alloys used as radioactive confinement boundary, To appear (2020).

[18] S. Chatzidakis, W. Tang, J. Chen, R. Miller, A. Payzant, J. Bunn, J. A. Wang, Neutron residual stress mapping of repaired spent nuclear fuel welded stainless-steel canisters, in: International High-Level Radioactive Waste Management 2019, IHLRWM 2019, 2019, pp. 249–253.

[19] S. Chatzidakis, S. Cetiner, H. Santos-Villalobos, J. J. Jarrell, J. M. Scaglione, Sensor requirements for detection and characterization of

stress corrosion cracking in welded stainless steel canisters, in: Proceedings of the 2018 International Congress on Advances in Nuclear Power Plants, ICAPP 2018, 2018, pp. 714–720.

[20] S. Chatzidakis, J. J. Jarrell, J. M. Scaglione, High-resolution ultrasound imaging using model-based iterative reconstruction for canister degradation detection, in: ANS IHLRWM 2017 - 16th International High-Level Radioactive Waste Management Conference: Creating a Safe and Secure Energy Future for Generations to Come - Driving Toward Long-Term Storage and Disposal, 2017, pp. 518–523.

[21] B. Lin, D. Dunn, R. Meyer, Evaluating the effectiveness of nondestructive examinations for spent fuel storage canisters, in: AIP Conference Proceedings, Vol. 2102, 2019. doi:10.1063/1.5099781.

[22] Dry canister storage system inspection and robotic delivery system development, Tech. rep., Electric Power Research Institute, Palo Alto, CA (2016).

[23] J. B. Renshaw, S. Chu, J. H. Kessler, K. Walldrop, Inspection and monitoring of dry canister storage systems, in: 15th International High-Level Radioactive Waste Management Conference 2015, IHLRWM 2015, 2015, pp. 824–828.

[24] M. Renshaw, Jeremy and Beard, Jamie and Stadler, Jim and Chu, Shannon and Orihuela, Robotically-deployed NDE inspection development for dry storage systems for used nuclear fuel, in: International Conference on the Management of Spent Fuel from Nuclear Power Reactors: Learning from the Past, Enabling the Future, Vienna, Austria, 2019.

[25] A. Chu, Shannon and Renshaw, Jeremy and Akkurt, Hatice and Csontos, Aging management for dry storage canisters, in: International Conference on the Management of Spent Fuel from Nuclear Power Reactors: Learning from the Past, Enabling the Future, Austria, Vienna, 2019.

[26] H. Jones, Jr. and Robert, Dry storage cask inventory assessment. Prepared for DOE, nuclear fuels storage and transportation planning project, Tech. rep., United States Department of Energy (2015).

[27] C. M. Yeum, S. J. Dyke, Vision-based automated crack detection for bridge inspection, Computer-Aided Civil and Infrastructure Engineering 30 (10) (2015) 759–770.

[28] L. I. Rudin, S. Osher, E. Fatemi, Nonlinear total variation based noise removal algorithms, Physica D: nonlinear phenomena 60 (1-4) (1992) 259–268.

[29] Y.-J. Cha, K. You, W. Choi, Vision-based detection of loosened bolts using the Hough transform and support vector machines, Automation in Construction 71 (2016) 181–188.

[30] M. O’Byrne, B. Ghosh, F. Schoefs, V. Pakrashi, Regionally enhanced multiphase segmentation technique for damaged surfaces, Computer-Aided Civil and Infrastructure Engineering 29 (9) (2014) 644–658.

[31] L. Wu, S. Mokhtari, A. Nazef, B. Nam, H.-B. Yun, Improvement of crack-detection accuracy using a novel crack defragmentation technique in image-based road assessment, Journal of Computing in Civil Engineering 30 (1) (2016) 4014118.

[32] Y. LeCun, L. Bottou, Y. Bengio, P. Haffner, Gradient-based learning applied to document recognition, Proceedings of the IEEE 86 (11) (1998) 2278–2324.

[33] J. B. Butcher, C. R. Day, J. C. Austin, P. W. Haycock, D. Verstraeten, B. Schrauwen, Defect detection in reinforced concrete using random neural architectures, Computer-Aided Civil and Infrastructure Engineering 29 (3) (2014) 191–207.

[34] D. Soukup, R. Huber-Mörk, Convolutional neural networks for steel surface defect detection from photometric stereo images, in: In-

ternational Symposium on Visual Computing, Springer, 2014, pp. 668–677.

[35] Y.-J. Cha, W. Choi, O. Büyüköztürk, Deep learning-based crack damage detection using convolutional neural networks, *Computer-Aided Civil and Infrastructure Engineering* 32 (5) (2017) 361–378.

[36] F. Chen, M. R. Jahanshahi, Nb-cnn: Deep learning-based crack detection using convolutional neural network and nave bayes data fusion, *IEEE Transactions on Industrial Electronics* 65 (5) (2018) 4392–4400.

[37] W. S. McCulloch, W. Pitts, A logical calculus of the ideas immanent in nervous activity, *The bulletin of mathematical biophysics* 5 (4) (1943) 115–133.

[38] B. Farley, W. Clark, Simulation of self-organizing systems by digital computer, *Transactions of the IRE Professional Group on Information Theory* 4 (4) (1954) 76–84.

[39] F. Rosenblatt, The perceptron: a probabilistic model for information storage and organization in the brain., *Psychological review* 65 (6) (1958) 386.

[40] K. Fukushima, Neocognitron: A self-organizing neural network model for a mechanism of pattern recognition unaffected by shift in position, *Biological cybernetics* 36 (4) (1980) 193–202.

[41] Y. LeCun, B. Boser, J. S. Denker, D. Henderson, R. E. Howard, W. Hubbard, L. D. Jackel, Back-propagation applied to handwritten zip code recognition, *Neural computation* 1 (4) (1989) 541–551.

[42] Y. LeCun, L. Bottou, Y. Bengio, P. Haffner, Gradient-based learning applied to document recognition, *Proceedings of the IEEE* 86 (11) (1998) 2278–2324.

[43] I. Goodfellow, Y. Bengio, A. Courville, Deep learning, MIT press, 2016.

[44] G. Cybenko, Approximation by superpositions of a sigmoidal function, *Mathematics of control, signals and systems* 2 (4) (1989) 303–314.

[45] L. Y. Pratt, Discriminability-based transfer between neural networks, in: *Advances in neural information processing systems*, 1993, pp. 204–211.

[46] K. He, X. Zhang, S. Ren, J. Sun, Deep residual learning for image recognition, in: *The IEEE Conference on Computer Vision and Pattern Recognition (CVPR)*, 2016.

[47] L. N. Smith, No more pesky learning rate guessing games, *CoRR*, [abs/1506.01186](https://arxiv.org/abs/1506.01186) 5 (2015).

[48] L. N. Smith, A disciplined approach to neural network hyper-parameters: Part 1–learning rate, batch size, momentum, and weight decay, *arXiv preprint arXiv:1803.09820* (2018).